ELECTRON TRANSPORT THROUGH AN "ANTIDOT" ARRAY

D. Weiss[1,2], M.L. Roukes[1], A. Menschig[3], P. Grambow[2]

[1]*Bellcore, Red Bank, New Jersey 07701*
[2]*Max Planck Institut für Festkörperforschung, D-7000 Stuttgart 80*
[3]*IV Physikalisches Institut der Universität Stuttgart, D-7000 Stuttgart 80*

An "anti"-dot array, geometrically complementary to a quantum-dot array, can be regarded as an artificial lattice of scatterers imposed upon a two dimensional conductor initially nearly devoid of intrinsic defects. This type of strong scattering potential, periodic on length scales short compared to the initial mean free path, has been realized in a high mobility two-dimensional electron gas through electron beam lithography and ion beam processing. Low temperature magnetotransport in such systems exhibits pronounced peaks in ρ_{xx} at low magnetic field with corresponding plateaus in ρ_{xy}. Contrary to results in weak periodic potentials, these features are *aperiodic* in $1/B$. This new structure occurs at fields where the cyclotron orbits are commensurate, i.e. can encircle a specific number of scatterers. We find that most features in ρ_{xx} and ρ_{xy} can be explained by an extended Drude model involving three distinct pools of carriers. Electrons on commensurate orbits pinned about a small number of "anti"-dots are not effective in transport and increase both, ρ_{xx} and ρ_{xy}.

I. INTRODUCTION

We study electron transport in a *periodic* lattice of impenetrable, circular potential barriers within a two-dimensional electron gas (*2DEG*). Ideally, one would expect that Bloch's theorem holds and that the electron motion is not affected by this lateral superlattice. Experimentally, however, the system behaves as a periodic array of scatterers, with an electron mean free path on the order of the period a. At zero magnetic field this behavior appears to reflect the fabrication induced roughness of the "anti"-dots on a length scale of order the Fermi wavelength which itself is a factor of five smaller than a. In an applied magnetic field this strong spatially modulated potential leads to dramatic commensurability effects at low temperatures. Pronounced structure is manifested in the magnetoresistance at low-B. We find that the predominant features can be explained classically, but many interesting, and anomalous, properties of this system appear beyond the scope of simple electron-orbit analysis.

Recently, it has been observed that magnetoresistance oscillations periodic in $1/B$ emerge at low magnetic fields when a high mobility *2DEG*

ISBN 0-12-409660-3

is subjected to a *weak* periodic 1*D* potential.[1] This phenomenon is attributed to the formation of Landau bands due to the soft lateral superlattice potential.[2-4] Preliminary work in 2*DEG* systems involving *strong* periodic potentials indicates that entirely different behavior is to be expected.[5-9] We shall explore this in detail below.

II. SAMPLES

The "anti"-dot samples are processed starting from high mobility GaAs-AlGaAs heterojunctions. At 4*K*, before "drilling" the holes, the densities range between $n_s \sim 2.2$ and $3.0 \times 10^{11} cm^{-2}$ and the mobilities are between $\mu_0 \sim 0.56$ to $1.2 \times 10^6 cm^2/Vs$. This corresponds to a transport mean free path, $\ell_0 = m^* v_F \mu_0 / e$, between 4.4 and 9.6 μm. Here, v_F is the Fermi velocity, and m^* the effective mass. A (square) lateral superlattice is introduced by etching an array of holes with lithographic diameters, d_{lith}, between 40 and 70 *nm* and with periods $a = 200$, and $a = 300$ *nm through* the 2*DEG* (Fig. 1, top inset). The "anti"-dot array is incorporated into a 100 μm wide Hall bar patterned from the 2*DEG* by conventional techniques (Fig.1, inset). The periodic array is defined by electron beam lithography (JEOL JBX5DII(U)) and transferred into the 2*DEG* by reactive ion etching.[10] An electron micrograph of a 300 *nm* period "anti"-dot array is displayed in Fig. 3. Although $\ell_0 >> a$, the Hall bar itself is *macroscopic*; its dimensions are large compared to ℓ_0. The device geometry with four potential probes on each side allows comparison of the resistivity (ρ_{xx}) and the Hall resistance (ρ_{xy}) from both patterned and unpatterned segments of the same sample.

III. EXPERIMENTAL RESULTS

The imposed array of "anti"-dots drastically affects transport at low-*B* as is demonstrated in Fig.1. The zero field resistivity, $\rho_{xx}(B = 0)$ is significantly higher in the patterned segment. Since the carrier density (determined from the periodicity of the Shubnikov-de Haas oscillations at higher fields) is comparable in both the pattened and the unpatterned area this reflects that the low-*B* mobility is strongly reduced ($\mu' = 4 \times 10^4 cm^2/Vs$). The corresponding mean free path ($\ell' \sim 0.34 \mu m$) has become comparable to *a*, the spacing between the imposed scatterers. When the magnetic field is increased the interplay between the two independent lengths, the cyclotron radius r_c and the imposed period *a*, results in striking commensurability effects: Low-field peaks dominate the magnetoresistivity ρ_{xx} (Fig. 1*a*), and are accompanied by (non-quantized) steps in ρ_{xy} (Fig.1*b*). The quenching of the Hall resistance, characteristic for *mesoscopic* junctions[11], is observed in our *macroscopic* Hall bar about $B = 0$ (Fig. 1*b*, inset). Arrows in Fig. 1, which closely correlate with these

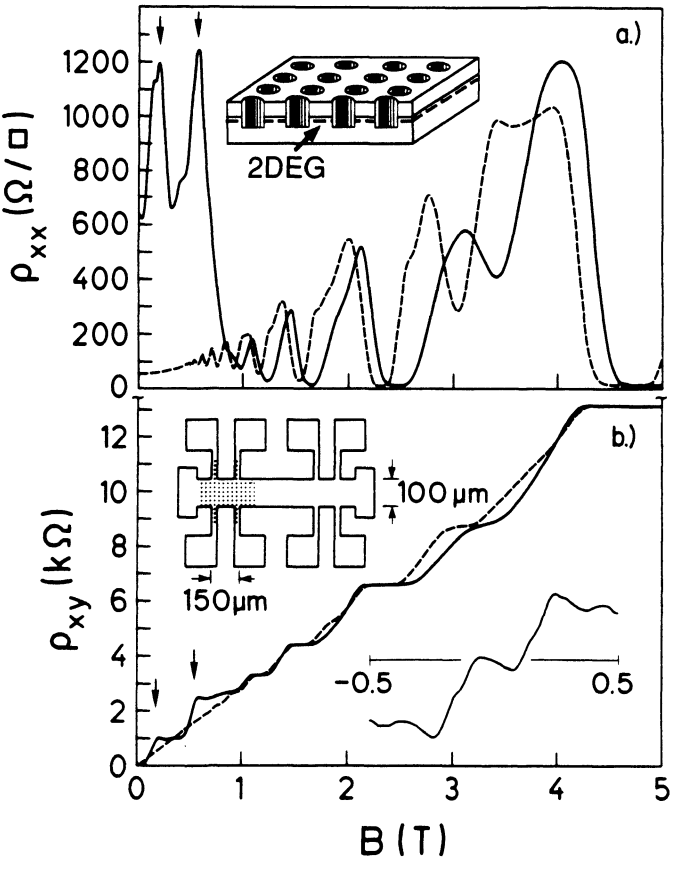

Figure 1. Magnetoresistance (a) and Hall resistance (b) measured in patterned (300 *nm* period, solid line) and unpatterned (dashed line) sample segments at 1.5K after brief illumination. In the patterned segment, n_s (determined from SdH-oscillations) is ~8% higher ($n_s = 2.4 \times 10^{11} cm^{-2}$). Top insets show a sketch of the "anti"-dot array and of the sample geometry. The bottom inset magnifies the quench in ρ_{xy} about $B = 0$. From Ref. 13.

features, mark field positions where the normalized cyclotron radius, $\hat{r}_c = r_c/a$, equals 1/2 and 3/2. When $\hat{r}_c < 1/2$, ρ_{xx} drops quickly, quantum oscillations commence and ρ_{xy} begins to display accurately quantized quantum Hall plateaus. In this high magnetic field regime traces from patterned and unpatterned segments become essentially identical. In the patterned area the spin-splitting of the first Landau-level ($n = 1$) at about 3.4 T remains resolved. This indicates that the intrinsic mobility between the etched holes is preserved after patterning.

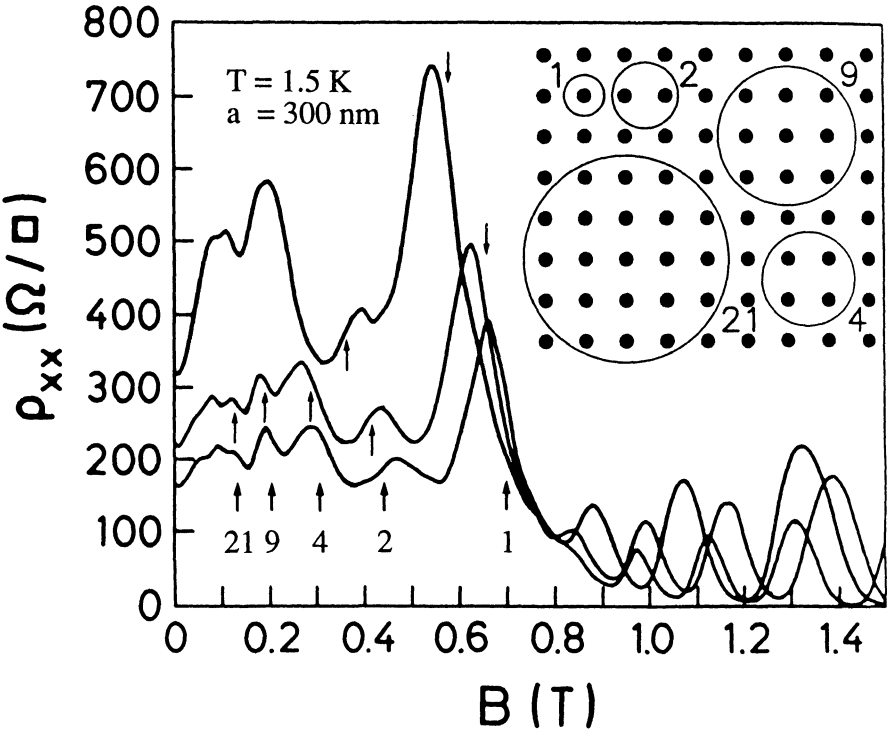

Figure 2. Low-B anomalies for one sample before (top trace) and after (lower two traces) brief illumination which increases n_s (2.8×10^{11} cm^{-2}, 3.7×10^{11} cm^{-2}, 4.05×10^{11} cm^{-2}, from top to bottom) and reduces ℓ_{depl}. Peaks in ρ_{xx} can be ascribed to commensurate orbits with $n = 1$, 2, 4, 9, 21; as sketched in the inset (for $\hat{d} = 1/3$ and average $\hat{r}_c = 0.5$, 0.8, 1.14, 1.7, 2.53; respectively) and marked by arrows. For the largest value of $\hat{d}$ (top trace) only a single peak at $\hat{r}_c = 3/2$ ($B = 0.19$ T) remains in place of the two peaks around $n = 4$, 9, seen in the lower traces.

The number of peaks and steps resolved in ρ_{xx} and ρ_{xy} depends upon the zero-field resistance, controlled by two parameters: the (normalized) "anti"-dot cross-section, $\hat{d} = d/a$, and the carrier density n_s. At low-B, ρ_{xx} is only weakly dependent upon the initial mobility μ_0 since the corresponding long mean free path ℓ_0 is "cut off" by the much shorter "anti"-dot spacing a. The *effective* cross-section of the extrinsic scatterers, $d = d_{lith} + 2\ell_{depl}$, involves the depletion length[12], ℓ_{depl}, itself dependent upon n_s. For our devices with the highest zero-field resistance only one peak (plateau) around $\hat{r}_c = 0.5$ can be observed.[13] The traces in Fig. 2, in contrast, are taken from the sample with the smallest d_{lith} (40 *nm*) and highest n_s (2.8×10^{11} cm^{-2}). Brief illumination of the samples at low

temperature further enhances n_s via persistent photoconductivity and reduces ℓ_{depl}.

Data taken after illumination (the two bottom traces in Fig. 2), involving the lowest $\rho_{xx}(B=0)$ and the smallest $\hat{d}$ (estimated to be $\sim 1/3$) merit special attention. This sample exhibits the largest sequence of peaks in ρ_{xx}, and corresponding plateaus in ρ_{xy} resolved so far. We find that the value of $\hat{r}_c$ at each peak can be associated with a particular commensurate orbit, marked by arrows. These special trajectories encircle a specific number, n, of "anti"-dots (Fig. 2, inset). This observation has lead us to the model presented below.

IV. "PINBALL" MODEL

The magnetotransport anomalies described above occur at low-B, in a regime where the cyclotron orbit diameters are larger or equal to the "anti"-dot spacing a. In this field regime, Landau quantization is suppressed in unpatterned samples when $T \geq 1.5K$ (Fig. 1*a*), while the microstructure-induced anomalies continue to be manifested up to temperatures $T \sim 50K$. This suggests that a classical description might account for the predominant structure. At low-B, when thermal broadening of the Landau levels is significant ($k_B T > \hbar\omega_c$), magnetotransport is described by the Drude model. In an ideal *unpatterned 2DEG*, with B applied normally, carriers perform cyclotron orbits with radius $r_c = v_F/\omega_c$ and angular frequency $\omega_c = eB/m^*$. For $\omega_c\tau < 2\pi$, scattering terminates the motion before a full orbit is completed. Here τ is the intrinsic momentum relaxation time, reflecting interactions between electrons and, e.g., intrinsic impurities, phonons, etc. For $\omega_c\tau >> 2\pi$, despite the circular trajectories, bulk current flows in the conductor since orbits drift with velocity $v_d = E_H/B$ in the Hall field, E_H, established. Within this classical picture the magnetoresistance is B-independent, $\rho_{xx} = m^*/n_s e^2\tau \equiv \rho_0$, and the Hall resistance rises linearly, $\rho_{xy} = B/n_s e \equiv R_0 B$ (R_0 is the Hall coefficient).

In the patterned areas we envision three types of carriers, differentiated by their trajectories in real space (right hand side, Fig. 3). At low magnetic fields, *pinned* and *scattered* orbits coexist: their relative fractions, however, strongly depend on the magnetic field. At higher fields $[\hat{r}_c < (\sqrt{2} - \hat{d})/2]$ the weight of these orbit types becomes neglegible and they are replaced by *drifting* orbits. Each of these different contingents (pinned, drifting, and scattered) can be characterized by their individual resistivities (ρ_p, ρ_d, ρ_s), and Hall coefficients (R_p, R_d, R_s) which contribute to the total magnetoresistance according to their B-dependent weights.

Pinned orbits are the key for understanding the striking

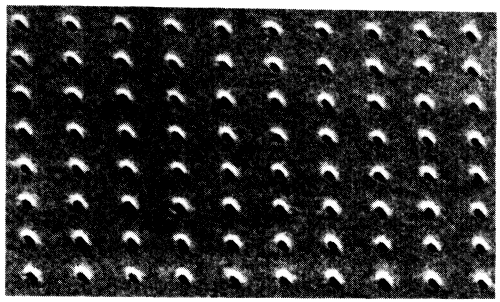

Figure 3. Electron micrograph of an "anti"-dot array ($a = 300nm$, tilted by 45°, left), and sketch of scattered (s), pinned (p), and drifting (d) electrons (right).

commensurability features seen in experiment. These "impaled" orbits arise at particular values of magnetic field when the repulsive potential of the symmetrically arranged neighboring "anti"-dots provides a local restoring potential against drift induced by external electric fields for specific cyclotron orbits. The fraction $f_p(\hat{r}_c)$ of electrons on pinned orbits can not contribute to the transport process and hence reduce the carrier density n_s for such commensurate magnetic fields. The "removal" of an electron from transport requires a long pinned orbit lifetime, $\tau_{pin} > a/v_F \sim \tau_{ex}$, obtained when μ_0 is preserved between "anti"-dots. At low-B, where $\hat{r}_c$ is large the current through the conductor is primarily carried by electrons which are *scattered* as in pinball. This fraction of carriers, $f_s(\hat{r}_c)$, scatters with an *effective* relaxation time $\tau' = (\tau^{-1} + \tau_{ex}^{-1})^{-1}$. Here, τ^{-1} and τ_{ex}^{-1} are the intrinsic and extrinsic rates. Transport coefficients for scattered carriers are thus $\rho_s = (\rho_0\tau)/(f_s\tau')$ and $R_s = R_0/f_s$. At high-B, however, it is *drifting* orbits, involving the fraction $f_d(\hat{r}_c)$ of carriers, which dominate transport. When the (normalized) cyclotron diameter becomes smaller than $1-\hat{d}$, backscattering is effectively suppressed and the carriers behave as if in an unpatterned sample; for them $\rho_d = \rho_0/f_d$ and $R_d = R_0/f_d$.[14] This suppression of backscattering for decreasing cyclotron orbit diameters is the origin of the striking negative magnetoresistance observed experimentally. The total resistivity and Hall coefficient are given by the inverted sum of the individual conductivity tensors, [13]

$$\frac{\rho}{\rho_0} = \frac{\tau(\tau' f_s + \tau f_d) + \tau'(\tau f_s + \tau' f_d)\omega_c^2\tau^2}{(\tau' f_s + \tau f_d)^2 + \tau'^2(1-f_p)^2\omega_c^2\tau^2} \qquad (1)$$

and

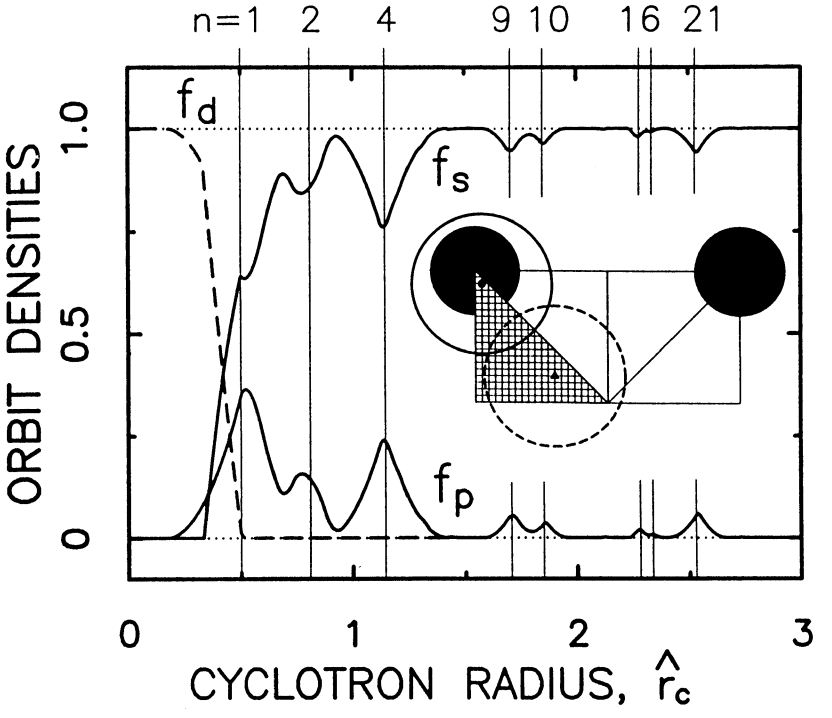

Figure 4. Calculated orbit densities vs. $\hat{r}_c$. Fine lines demark average $\hat{r}_c$-values of orbits impaled upon $n = 1,2,4,9,10,16$, and 21 "anti"-dots. The inset shows one half of the real space unit cell. By symmetry, calculations need only be carried out for one eighth of the unit cell, as shown. As an example, two orbit centers for $\hat{r}_c = 0.3$, represented by two symbols on the coarse grid shown, are found to correspond to a pinned orbit (solid line) and a drifting orbit (dashed line).[14]

$$\frac{R}{R_0} = \frac{\tau'^2 f_s + \tau^2 f_d + \tau'^2(1-f_p)\omega_c^2\tau^2}{(\tau' f_s + \tau f_d)^2 + \tau'^2(1-f_p)^2\omega_c^2\tau^2}. \tag{2}$$

These expressions explicitely relate transport coefficients to the $\hat{r}_c$-dependent orbit densities and scattering rates. The scattering rates τ and τ' can be estimated experimentally from the zero-field resistance of unpatterned and patterned devices; the orbit densities, however, have to be calculated.

V. CALCULATION OF ORBIT DENSITIES

In order to qualitatively model the magnetoresistance, we have set up a straightforward calculation to determine the $\hat{r}_c$-dependent fractions, f. We

describe the "anti"-dots by circular hardwall potentials rising from the elsewhere homogeneous *2DEG*. In this approximation, applicable when $\ell_{depl} << a - d_{lith}$ (and especially relevant for the data of Fig. 2) electrons interact with the fabrication-imposed electrostatic potential only in the immediate locale of each "anti"-dot; elsewhere carriers move freely in the applied fields. This assumption precludes the complicated and chaotic electron trajectories[15] which can arise in a more realistic, quasi-specular, periodic potential. The *f's* are calculated numerically. At each value of $\hat{r}_c$ we calculate the fraction of pinned electron orbits (completed, enclosing one or more "anti"-dots), drifting orbits (completed, without enclosing "anti"-dot), and scattered orbits (uncompleted) with centers on a grid of $\sim 10^5$ sites within the real-space unit cell (sketched schematically with a much coarser grid in the inset of Fig. 4). In Fig. 4 orbit densities calculated for $\hat{d} = 1/3$ are seen to display pronounced commensurability effects. For increasing values of $\hat{d}$ both experiments[13] and calculations[16] show that structure for $n > 1$ becomes suppressed.

VI. "THEORY" vs. EXPERIMENT

We compare calculated results to experimental data in Fig. 5. Here we have assumed that the effective mean free path of scattered electrons, $\ell' = v_F \tau'$ is $\hat{r}_c$-independent. Remarkable similarities are evident: $n = 1$, 2, and 4 commensurability effects are prominent in both ρ_{xx} and ρ_{xy}. In the experimental trace, surprisingly, we find clearly resolved $n = 9$ and 21 features. Our calculations predict these to be quite weak, even for smaller $\hat{d}$. We attribute their enhancement in real samples to the finite potential gradient between "anti"-dots. This should act to "guide" electrons around the "anti"-dots, permitting deviations from strictly circular trajectories (as assumed in the model) and enhancing f_p. For samples with larger cross-sections $\hat{d}$ the potential gradient between "anti"-dots is expected to be significant. This characteristic is outside the scope of assumptions made in our simple model. Peaks experimentally observed at $\hat{r}_c \sim 3/2$ in Fig. 1 and Fig. 2 are, in fact, strongly forbidden for strictly *circular* orbits when $\hat{d} \geq 1/3$. Despite the more complicated dynamics in real samples, however, we believe our simple "billiard"-like approach elucidates the basic origin of the dominant structure observed in experiments.

VII. SPECULAR vs. DIFFUSE SCATTERING FROM "ANTIDOTS"

Data at low magnetic field show a clear quenching of the Hall effect. By contrast, this behavior is absent in our calculated traces. Experiments in *mesoscopic* junctions[11], and subsequent theory[17], indicate that quenching is a classical phenomenon requiring a component of specular reflection from the boundaries. Theory and experiment have clearly

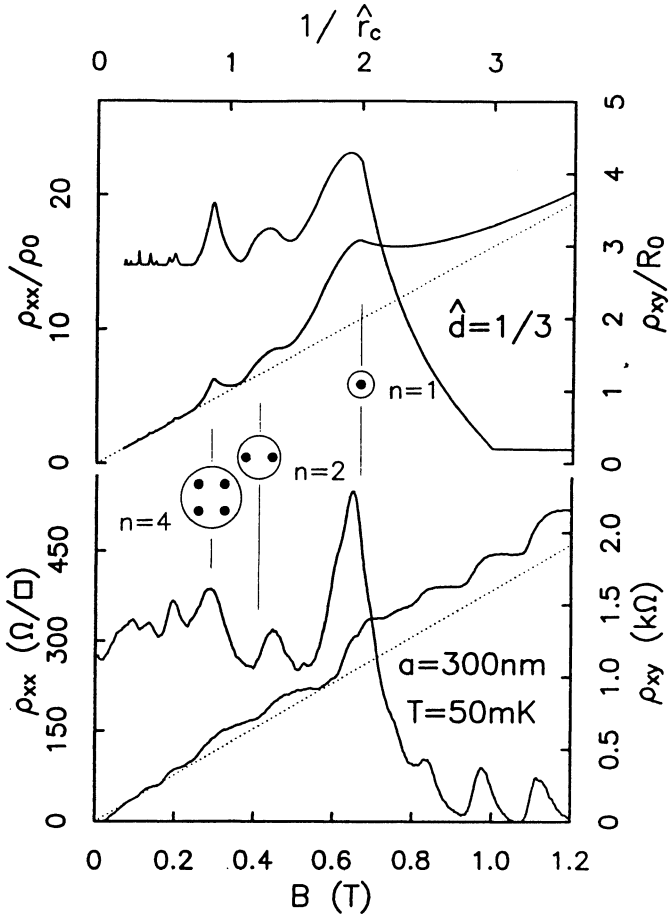

Figure 5. Comparison between the simple model *(top)* and experiment *(bottom)*. Calculated curves are obtained assuming a *constant* effective mean free path for extrinsically scattered carriers, $\ell'/a \sim 2.4$, and an intrinsic value $\ell/a \sim 33$ (values taken from experiment). Features attributed to $n = 1$, 2, and 4 pinned orbits are denoted. Very weak temperature dependence is observed experimentally for $50mK < T < 4.2K$. From Ref. 13.

demonstrated that strictly *zero*, even negative, low-B Hall coefficients are possible in the ballistic regime. Here, however, our extensions of the Drude model implicitly involve a relaxation-time approximation for extrinsic collisions. This is valid when scattering from the "anti"-dots is completely *diffuse*. This assumption clearly precludes accounting for phenomena, such as quenching, involving correlated multiple reflections.

Despite these simplifying assumptions, the results from our model agree rather well with experiment (Fig. 5). This agreement appears to emphasize the fact that quenching and the low-B commensurability effects originate from different mechanisms.

VIII. PROJECTIONS

Quantum behaviour should leave its mark with further reduction of the lattice constant. If only a few flux quanta h/e penetrate the unit cell $a \times a$ exotic consequences are expected in transport due to the self-similar energy spectrum.[18] Manifestations of this irregular spectrum have recently been obtained from samples with weak periodic potentials.[19] Further advances in microfabrication of *2DEG* heterojunctions will enable explorations deep within this regime.

ACKNOWLEDGEMENTS

We thank K. von Klitzing, R. R. Gerhardts, A. Forchel and O. Alerhand for valuable discussions, G. Weimann for providing the samples S. Koch for assistance with *mK* measurements, and M. Riek and E. Vasiliadou for technical contributions.

REFERENCES

1) D. Weiss *et al.*, Europhys. Lett. **8**, 179 (1989).
2) R. R. Gerhardts, D. Weiss, and K. von Klitzing, Phys. Rev. Lett. **62**, 1173 (1989).
3) R. W. Winkler, J. P. Kotthaus, and K. Ploog, Phys. Rev. Lett. **62**, 1177 (1989)
4) E. S. Alves, *et al.*, J. Phys.: Condens. Matter **1**, 8252 (1989)
5) M. L. Roukes, and A. Scherer, Bull. Am. Phys. Soc. **34**, 633 (1989); A. Scherer and B. P. van der Gaag, Proc. SPIE **1284**, 149 (1990).
6) C. G. Smith, *et al.*, J. Phys.: Condens. Matter **2**, 3405 (1990)
7) H. Fang and P. J. Stiles, Phys. Rev. **B41**, 10171 (1990)
8) K. Ensslin and P. M. Petroff, Phys. Rev. **B41**, 12307 (1990)
9) J. P. Kotthaus, In "*Granular Nanoelectronics*", (Plenum, London, 1990)
10) D. Weiss *et al.*, Appl. Phys. Lett. **58**, 2960 (1991)
11) M.L. Roukes *et al.*, Phys. Rev. Lett. **59**, 3011 (1987); **64**, 1154 (1990).
12) A. Scherer and M.L. Roukes, Appl. Phys. Lett. **55**, 377 (1989); T. Demel *et al., ibid.* **53**, 2176 (1988).
13) D. Weiss *et al.*, Phys. Rev. Lett. **66**, 2790 (1991)
14) At high-B, a drifting electron encountering an "anti"-dot will briefly

skip about its periphery. Its orbit center then precesses, step-wise, to the back side where it is ultimately freed, once again, to drift away. Here, we assume a short dwell time and equate skipping to drifting orbits.

15) In related work, T. Geisel, *et al.*, Phys. Rev. Lett. **64**, 1581 (1990), describe chaotic classical dynamics.

16) M.L. Roukes, *unpublished.*

17) C.W.J. Beenakker and H. van Houten, Phys. Rev. Lett. **63**, 1857 (1989).

18) P. G. Harper, Proc. Phys. Soc. **A 68**, 874 (1955); M. Ya. Azbel, Sov. Phys. JETP **19**, 634 (1964); D. R. Hofstadter, Phys. Rev. **B14**, 2239 (1976)

19) R. R. Gerhardts, D. Weiss, and U. Wulf, Phys. Rev. **B43**, 5192 (1991); D. Weiss *et al.*, EP2DS-9 Proceedings, Nara, Japan 1991, [Surf. Sci. (to be published)]